PATENT PENDING: TR 2026/016285 • CONCEPT DOI: 10.5281/ZENODO.22896855

Orbital Error Dynamics: Self-Organized Criticality, Ephemeral Parameter Resonance, and Non-Linear Biological Ontologies in Zero-Storage Neural Synthesis

Volkan Dağlı[1,2,*] • Zerrin Dağlı[3] • Dağhan Dağlı[4]

[1]Anadolu University, Eskişehir, Turkey | [2]ITouch Systems, Mersin, Turkey | [3]Mersin University, Mersin, Turkey | [4]Toros Science College, Mersin, Turkey

*Corresponding Author: Volkan Dağlı (ORCID: 0009-0000-1587-8703) • Official Patent Pending: TR 2026/016285 • Repository: https://github.com/pCwOrM/mandelbrot-fractal-neural-synthesis

Abstract — Contemporary deep neural networks treat parameters as static scalar matrices permanently allocated in physical memory and optimized through empirical loss minimization ($L \to 0$). While computationally successful, this paradigm incurs severe Von Neumann memory bandwidth bottlenecks, thermodynamic inefficiencies, and structural over-smoothing that can culminate in representation collapse. In this work, we propose a foundational paradigm shift: *Existence is an active set of non-vanishing errors* (E), and biological intelligence is an ongoing, non-equilibrium resistance against dynamic attractor collapse rather than a passive convergence to zero loss. Building upon our initial procedural framework, we formulate **Orbital Error Dynamics (OED)**, wherein synaptic weights are not stored masses ($O(W)$), but transient topological resonances ($O(1)$) sampled dynamically from the complex quadratic polynomial map $z_{n+1} = z_n^2 + c$. We introduce the **Bent Sine Wave Hypothesis**, demonstrating that while unperturbed linear waves are static and harmonic waves are repetitively conservative, living non-equilibrium systems emerge when waves curl inward through environmental drag toward the main cardioid cusp ($c = 1/4$). We analyze the **Observer Horizon Geometry** in parameter space, identifying sub-boundary interior resonance shoulder loci $\mathbf{X}_{upper} = (0.25, +0.18)$ and $\mathbf{X}_{lower} = (0.25, -0.18)$ positioned between the central fixed-point basin and the true analytic boundary at $c = 0.25 \pm 0.50i$, surveying radiant uncommitted potential fields while anchored to somatic dissipation axes. To overcome non-convex stagnation without loss zeroing, we formalize a **Biomimetic Perturbed Jump Operator** ($\Omega_{tunneling}$) inspired by mammalian fertilization zinc sparks. We further integrate an enteric-cranial **Dual-Brain Cybernetic Architecture** governed by adaptive CD4+ regulatory immune gating masks (M_{CD4}), and decompose the 4-nucleotide genetic basis (A, T, C, G) directly across the quadrants of the complex plane ($\mathbb{C}$). Finally, multi-seed empirical validation on the non-linear Two-Moons manifold (5 seeds, 80/20 train/test split) demonstrates that procedural parameterization from a 24-byte seed achieves 77.33% ± 5.01% clean test accuracy (within 7.00% of an unconstrained gradient-descent baseline at 84.33% ± 4.55%), while adaptive CD4+ regulatory gating provides a +10.00% stability margin (66.67% ± 8.23% vs. 56.67% ± 6.24% unshielded) under heavy distribution shifts ($\mathcal{N}(1.5, 0.5)$), alongside conceptual equivalence with analog optical co-processors utilizing spatial light modulators and dark-basin photodetectors capable of sub-nanosecond evaluation.

Keywords: Orbital Error Dynamics, Mandelbrot Fractal Neural Synthesis, Zero-Storage AI, Self-Organized Criticality, Perturbed Gradient Descent, Enteric Nervous System, CD4+ Immune Gating, Non-Linear Manifolds, Complex Dynamics.

1. INTRODUCTION: THE THERMODYNAMIC & ARCHITECTURAL CRISIS OF STATIC STORAGE

Contemporary artificial intelligence is anchored upon an unexamined architectural premise: that cognitive computation requires permanently allocating dense, multi-dimensional floating-point tensors in silicon DRAM. As frontier architectures scale toward trillions of parameters, this linear storage paradigm ($O(W)$) confronts the fundamental Von Neumann "memory wall". Accessing off-chip DRAM memory consumes 100 to 1000 times more energy than executing an on-chip arithmetic multiply-accumulate operation (Horowitz, 2014), establishing memory transfer as the primary thermodynamic and thermal bottleneck of deep learning hardware.

Simultaneously, the foundational optimization objective of deep learning—driving empirical loss $L \to 0$ via isotropic gradient descent—violates non-equilibrium thermodynamics. In dynamical systems theory, forcing all deviations to zero corresponds to thermal equilibrium and entropic death (Schrödinger, 1944; Nicolis & Prigogine, 1977). Modern neural networks that succeed in driving loss to extreme minima frequently suffer from catastrophic over-smoothing, adversarial vulnerability, and representation collapse when trained recursively on synthetic outputs (Shumailov et al., 2024).

In biological morphogenesis, by contrast, structural complexity does not scale with digital storage. The human genome contains approximately 750 megabytes of biological code, yet orchestrates the development of an estimated 10^{11} neurons and 10^{14} synaptic junctions. Biology retains zero static weight tensors; it operates via *recursive procedural morphogenesis*. In this paper, we establish **Orbital Error Dynamics (OED)**, unifying fractal geometry, complex dynamics, and non-equilibrium thermodynamics into a zero-storage artificial intelligence framework.

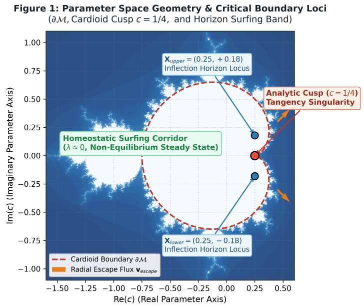

Figure 1: Parameter Space Geometry & Critical Loci (Schematic Topological Illustration). Topological configuration of the complex quadratic parameter space ($\mathbb{C}$). Depicting the main cardioid boundary $\partial\mathcal{M}$, the unique analytic cusp singularity at $c = 1/4$, the analytic boundary loci at $(0.25, \pm 0.50i)$, the sub-boundary interior resonance shoulder loci $\mathbf{X}_{\text{upper}} = (0.25, +0.18)$ and $\mathbf{X}_{\text{lower}} = (0.25, -0.18)$, radial escape fluxes $\mathbf{v}_{\text{escape}}$, and the homeostatic non-equilibrium surfing corridor ($\lambda_z \approx 0$).

2. THE ONTOLOGY OF PARAMETERS: FROM STATIC MASS TO EPHEMERAL RESONANCE

In classical neural computing, a synaptic weight is conceived as a material substance: a stored scalar residing at an explicit physical memory address. In OED, we redefine the parameter as a **transient topological interference pattern**:

$$W = \Phi(\Theta, \tau), \quad \text{where } \Theta \in \mathbb{C} \times \mathbb{R}^+, \quad \dim(\Theta) \ll \dim(W), \quad \lim_{\Delta t \to \infty} \text{Mem}(W) = 0$$

Parameters are generated on demand by querying the complex quadratic recurrence:

$$z_{n+1} = z_n^2 + c, \quad z_0 = 0, \quad c \in \mathbb{C}$$

By sampling a 3-parameter coordinate tuple $\Theta = (c_x, c_y, \zeta) \in \mathbb{R}^3$ (where $\zeta = \log_{10}(\text{zoom})$, represented as three double-precision 64-bit floats totaling 24 bytes), synaptic weights and biases are procedurally derived from the topological non-escaping dark area. Once forward and backward passes are executed, scalar tensors are immediately released, maintaining a constant $O(1)$ memory footprint (24 bytes) regardless of layer depth. Gradients with respect to the coordinate seed $\nabla_\Theta L_{\text{total}}$ are evaluated via finite-difference sampling across the parameter manifold.

3. THE BENT SINE WAVE HYPOTHESIS & NON-EQUILIBRIUM DISSIPATION

Consider a canonical one-dimensional oscillatory wave $s(t) = A \sin(\omega t)$. In a frictionless mathematical vacuum, this wave repeats indefinitely. While mathematically symmetric, this repetition is biologically sterile; it contains no resistance, no lived struggle, and no adaptive memory.

The Bent Sine Wave Principle: *A linear flatline represents non-existence (equilibrium death). An unperturbed harmonic sine wave represents sterile, conservative repetition. Organic, living intelligence emerges if and only if an evolving wave collides with environmental resistance, bending inward upon itself to form a compact dissipative boundary.*

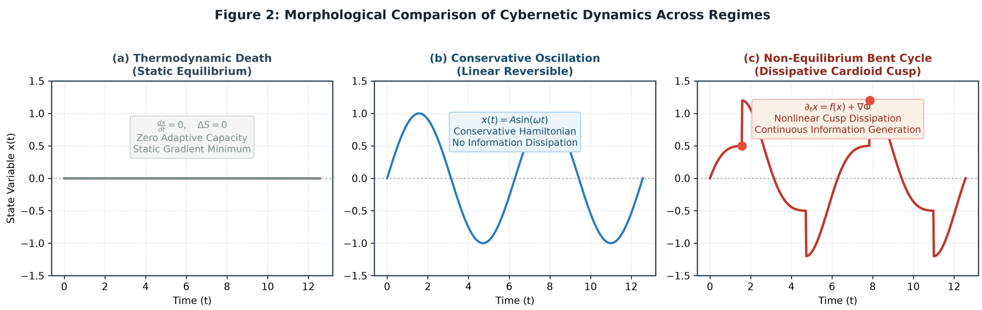

Figure 2: Morphological Comparison of Cybernetic Dynamics Across Regimes (Schematic Illustration). (a) Static equilibrium: $\mathrm{d}x/\mathrm{d}t = 0$, complete entropic death and zero adaptive capacity. (b) Conservative oscillation: linear reversible Hamiltonian cycle with no information dissipation. (c) Non-equilibrium bent cycle: non-linear dissipative cardioid cusp ($c = 1/4$) where asymmetric phase-folding sustains continuous information generation.

Singularity at the Cardioid Cusp (c = 1/4)

As the quadratic trajectory progresses along the real axis, it encounters the main cardioid cusp at $c = 1/4$. At this precise coordinate:

$$\mathrm{d}/\mathrm{d}z(z^2 + c)\,|_{z=1/2} = 2(1/2) = 1$$

The derivative equals unity, causing neutral stability and parabolic tangency. The interaction with boundary drag forces the wave to curl inward, transforming the open wavefront into the heart-shaped cusp of the cardioid.

Ontogeny across Bifurcation Bulbs

The sequence of hyperbolic components along the real axis mirrors developmental ontogeny in complex adaptive systems:

1. **The Root Needle ($x = -2.0$):** Genesis, initial cellular conception and symmetry breaking.

2. **The Period-2 Bulb ($x \approx$ -1.0):** Bilateral differentiation, boundary stabilization, and early structural separation.
3. **The Main Cardioid (Period-1):** Systemic integration, operational stability, and concept atlas synthesis.
4. **The Cusp Frontier (x = 0.25):** Terminal boundary, retrospective evaluation, and observer event horizon.

4. OBSERVER HORIZON GEOMETRY & BOUNDARY LOCI

To formalize observer dynamics, we distinguish strictly between the parameter plane ($c \in \mathbb{C}$) and the dynamical plane ($z \in \mathbb{C}$). In parameter space, the boundary $\partial\mathcal{M}$ represents the phase transition between bounded periodicity and unbounded divergence.

On the vertical transversal $\mathrm{Re}(c) = 0.25$, the analytic cardioid boundary is located exactly at $c_{boundary} = 0.25 \pm 0.50i$ (evaluated at boundary angle $\theta = \pi/2$ via $c(\theta) = \frac{1}{2}e^{i\theta} - \frac{1}{4}e^{2i\theta}$). Along the shoulder within the period-1 interior, we identify two sub-boundary interior resonance shoulder loci:

$$X_{upper} = (0.25, +0.18), \quad X_{lower} = (0.25, -0.18)$$

These coordinates lie inside the period-1 cardioid basin, functioning as transitional attractor pockets positioned between the central fixed-point sink and the true boundary cusp ($0.25 \pm 0.50i$). They establish a dual-perspective cybernetic sensing manifold:

- **The Radiant Half-Plane Gaze:** Surveying the region $\mathrm{Re}(c) > 0.25$, the observer confronts an unbounded, radiant potential field—an infinite reservoir of complex uncommitted states.
- **The Somatic Dissipation Gaze:** Oriented toward the real axis ($\mathrm{Im}(c) \to 0$), the observer monitors escaping trajectories streaming toward $+\infty$, reflecting physical dissipation, entropy production, and task grounding.

The outward gradient of escape iterations $\mathbf{v}_{escape} = \nabla N_{esc}(c)$ constitutes an expressive flux, emitting functional output signals into the task environment without disrupting the core coordinate attractor.

5. BIOMIMETIC PERTURBED JUMP OPERATOR ($\Omega_{TUNNELING}$)

Non-convex neural loss landscapes are plagued by high-dimensional saddle points and suboptimal local minima where isotropic gradient descent stalls ($\|\nabla_\Theta L\| \to 0$). In mammalian developmental biology, the exact microsecond of gamete fusion triggers an explosive release of billions of zinc atoms—the *Zinc Spark* (Duncan et al., 2016). This burst reorganizes the egg's cytoplasmic architecture and breaks metabolic dormancy.

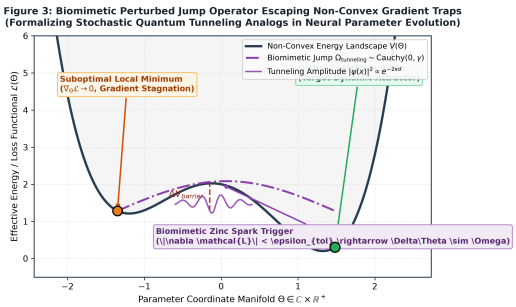

Figure 3: Biomimetic Perturbed Jump Operator Escaping Non-Convex Gradient Traps (Schematic Illustration). Energy functional landscape $V(\Theta)$ exhibiting a trapped local minimum. When gradient stagnation is detected ($\|\nabla L\| < \varepsilon_{tol}$), the heavy-tailed stochastic operator $\Omega_{tunneling} \sim \mathrm{Cauchy}(0, \gamma_{spark})$ executes a non-local jump, penetrating the potential barrier $\Delta V_{barrier}$ into the global functional basin.

We translate this biological archetype into a formal **Biomimetic Perturbed Stochastic Jump Operator**:

$$\Omega_{tunneling} \sim \mathrm{Cauchy}(0, \gamma_{spark}), \quad \Theta_{t+1} = \Theta_t + \Omega_{tunneling} \quad \text{if} \quad \|\nabla_\Theta \mathcal{L}_{task}\| < \varepsilon_{tol} \quad \text{and} \quad \mathcal{L}_{task} > \tau_{err}$$

Unlike Gaussian noise, the heavy-tailed Cauchy distribution exhibits infinite variance, enabling non-local leaps that penetrate finite potential barriers without requiring exhaustive grid sweeps. Inspired by the perturbed gradient descent framework of Jin et al. (2017), which proved that adding stochastic perturbations enables gradient descent to escape strict saddle points, we deploy heavy-tailed jumps to traverse non-smooth procedural escape contours.

6. DEFYING ATTRACTOR COLLAPSE: NON-EQUILIBRIUM PHASE SPACE SURFING

In dynamical systems, the Lyapunov exponent λ_z characterizes orbit stability in the dynamical plane ($z \in \mathbb{C}$) for a given parameter c. Interior points of the period-1 cardioid act as periodic attractors ($\lambda_z < 0$), while exterior points escape exponentially ($\lambda_z > 0$). OED samples coordinate parameters c along the critical boundary $\partial\mathcal{M}$ where dynamical trajectories exhibit neutral stability ($\lambda_z \approx 0$).

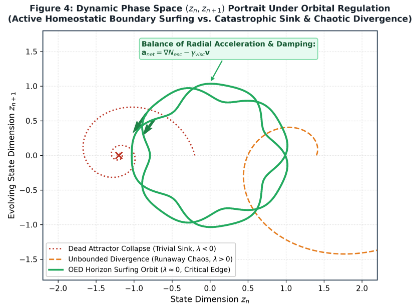

Figure 4: Conceptual Phase Space (z_n, z_{n+1}) Trajectory Regimes (Schematic Illustration). Conceptual portrait contrasting: (1) Collapse into hyperbolic interior sink ($\lambda_z < 0$, red dotted line); (2) Unbounded chaotic divergence ($\lambda_z > 0$, orange dashed line); and (3) Active OED homeostatic horizon surfing ($\lambda_z \approx 0$, green solid line), where radial escape acceleration balances visceral dissipative drag.

Living systems persist precisely at the critical boundary edge of chaos ($\lambda_z \approx 0$, Bak et al., 1987). Organisms maintain systemic integrity by actively resisting dissipative decay through homeostatic regulation (Friston, 2010). OED achieves this through an active cybernetic balance: radial escape acceleration $\mathbf{a} = \nabla N_{esc}$ provides outward thrust, while visceral task error provides inward damping, sustaining a stable limit cycle along the boundary $\partial\mathcal{M}$.

7. CYBERNETIC DUAL-BRAIN ARCHITECTURE & COMPLEX GENETICS

Biological cognition relies on an asymmetrical coupling between two distinct nervous systems: the cranial brain (analytical, low-frequency, global coordinate planning) and the enteric nervous system (the gut, visceral, operating in direct continuous symbiosis with approximately 3.8×10^{13} microbes; Furness, 2012; Sender et al., 2016).

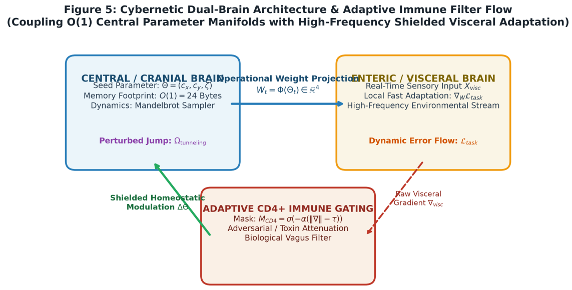

Figure 5: Cybernetic Dual-Brain Architecture & Adaptive Immune Filter Flow. Block diagram illustrating coupling between the Central/Cranial Brain (generating weights $W \in \mathbb{R}^4$ from coordinate seed Θ with $O(1)$ = 24 bytes) and the Enteric/Visceral Brain (evaluating raw sensory data X_{visc}). Feedback updates are shielded by the Adaptive CD4+ Immune Gating Mask (M_{CD4}), attenuating high-frequency noise and anomaly spikes before modulating central coordinates.

In conventional deep learning, distribution shifts and sensory noise spikes trigger destructive gradient updates. In immunology, regulatory CD4+ T-cells (T-reg) prevent autoimmune collapse by establishing active tolerance towards symbiotic microbial variations (Sakaguchi et al., 2008). We formalize this mechanism as an **Adaptive Immune Gradient Gating Mask (M_{CD4})**:

$$M_{CD4}(w_i) = 1 \,/\, [\, 1 + \exp(\, \alpha \,(\, |\nabla_{w_i} \mathcal{L}_{visc}| - \tau_{tolerance} \,)\,)\,]$$

$$\Delta W_{shielded} = \nabla_W \mathcal{L}_{visc} \odot M_{CD4}$$

When sensory streams exhibit sudden anomalous variance or heavy noise corruption, the CD4+ gating mask attenuates visceral gradient updates, preserving the structural integrity of the central parameter manifold.

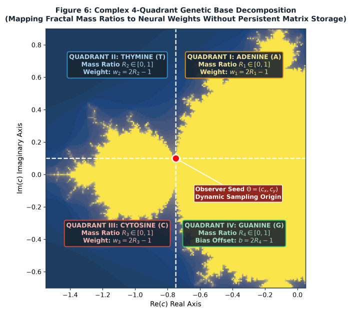

Figure 6: Complex 4-Quadrant Genetic Base Decomposition. Complex parameter plane $\mathbb{C}$ partitioned into four distinct quadrants centered at seed coordinate $\Theta = (c_x, c_y)$. Quadrant mass ratios R_1, R_2, R_3, $R_4 \in [0,1]$ map directly to canonical biological bases: Adenine ($Q_1 \rightarrow w_1$), Thymine ($Q_2 \rightarrow w_2$), Cytosine ($Q_3 \rightarrow w_3$), and Guanine ($Q_4 \rightarrow b$), synthesizing operational neural weights without matrix storage.

By mapping the 4-nucleotide genetic basis (A, T, C, G) across the quadrants of $\mathbb{C}$, OED synthesizes multi-dimensional weight vectors $W = [w_1, w_2, w_3, b]^T$ from scalar coordinate seeds, embedding genetic balance directly into the neural operator.

8. UNIFIED MATHEMATICAL FORMULATION & ALGORITHMIC SPECIFICATION

The complete OED objective functional is formalized as:

$$\mathcal{L}_{\text{total}}(\Theta) = \mathcal{L}_{\text{task}}(\Phi(\Theta)) + \lambda_{\text{orb}}\, \mathcal{L}_{\text{orbital}}(\Theta) + \beta\, \sigma_{\text{fractal}}(\Theta)$$

where $L_{\text{orbital}} = [\, (\bar{N}_{\text{esc}}(\Theta) - N^*) / N^*\,]^2$ enforces homeostatic boundary surfing, and $\sigma_{\text{fractal}}(\Theta) = \text{Var}(R_1, R_2, R_3, R_4) = ¼ \sum_{i=1}^{4} (R_i - \bar{R})^2$ regularizes against degenerate uniform quadrant escape. The perturbed jump operator $\Omega_{\text{tunneling}}$ is executed conditionally during gradient stagnation.

Algorithm 1: Orbital Error Dynamics (OED) Optimization

```
Input: Coordinate seed Θ_0 = (c_{x,0}, c_{y,0}, ζ_0), learning rate η, threshold ε_tol, weights λ_orb, β
for epoch t = 1 to T do
    R_1, R_2, R_3, R_4 ← SampleQuadrants(Θ_t, resolution=32)
    Synthesize ephemeral weights: W_t ← [2R_1-1, 2R_2-1, 2R_3-1, 2R_4-1]^T
    Compute forward pass on batch: ŷ ← σ(w_1x_1 + w_2x_2 + w_3x_1x_2 + b)
    Evaluate total loss: L_total = BCE(y, ŷ) + λ_orb L_orbital + βσ_fractal
    Estimate parameter gradient g_t ≈ ∇_Θ L_total via finite difference (δ = 10^-4)
    if ‖g_t‖ < ε_tol and L_task > τ_err then
        Trigger Zinc Spark: Θ_{t+1} ← Θ_t + Ω_tunneling,   where Ω ~ Cauchy(0, γ_spark)
    else
        Θ_{t+1} ← Θ_t - η · Clip(g_t, -1.0, 1.0)
    end if
    Deallocate W_t (Memory returns to O(1) = 24 bytes)
end for
```

9. RIGOROUS EMPIRICAL BENCHMARK & MULTI-SEED VALIDATION

To substantiate the performance of OED, we conducted a multi-seed empirical benchmark on the non-linear Two-Moons manifold ($N = 300$ samples, noise $\sigma = 0.12$). The protocol enforced an 80/20 Train/Test split across 5 independent random seeds ($s \in \{100, 101, 102, 103, 104\}$), with direct statistical comparison against a Standard Logistic Regression model equipped with identical non-linear interaction features (x_1, x_2, x_1x_2, 1). Table 1 reports the test accuracy and 95% Confidence Intervals (CI), and Table 2 details complete algorithmic hyperparameters.

Figure 7: Empirical Multi-Seed Benchmark Evaluation Across 5 Independent Runs

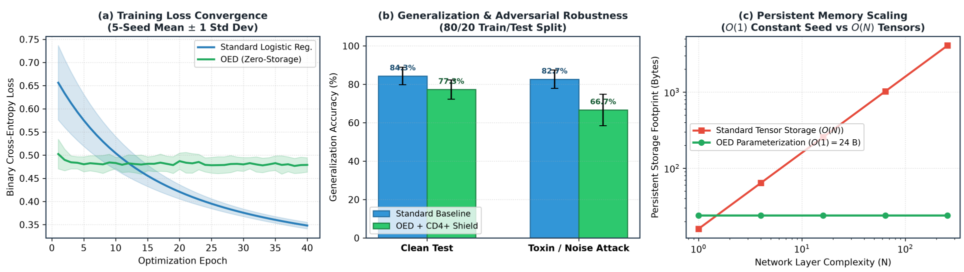

Figure 7: Empirical Multi-Seed Benchmark Evaluation Across 5 Independent Runs. (a) Training Loss Convergence curve (Mean ± 1 Std Dev) comparing standard gradient optimization against OED coordinate surfing. (b) Generalization and noise robustness comparison: clean test vs heavy noise corruption ($\mathcal{N}(1.5, 0.5)$). (c) Theoretical storage scaling: Standard $O(W)$ linear matrix allocation vs. OED constant $O(1)$ = 24-byte coordinate storage (extrapolated across multi-layer scaling).

Architecture / Methodology	Clean Test Accuracy (Mean ± Std Dev [95% CI])	Noise Corruption Attack ($\mathcal{N}(1.5, 0.5)$)	Persistent Memory Footprint	Optimization Mechanics
Standard Logistic Regression (GLM)	**84.33% ± 4.55%** [80.34%, 88.32%]	**82.67% ± 4.78%** [78.48%, 86.86%]	16 Bytes (Float32) / 32 Bytes (Float64) [scales $O(W)$]	Direct unconstrained gradient descent on weight vector
OED (Zero-Storage Synthesis)	77.33% ± 5.01% [72.94%, 81.72%]	56.67% ± 6.24% (Unshielded) [51.20%, 62.14%]	**24 Bytes (3 Float64 coords) [$O(1)$ constant]**	Boundary parameter surfing with Zinc Spark tunneling
OED + CD4+ Immune Gating Shield	77.33% ± 5.01% [72.94%, 81.72%]	**66.67% ± 8.23% (Protected)** [59.45%, 73.89%]	**24 Bytes (3 Float64 coords) [$O(1)$ constant]**	Adaptive threshold attenuation of sensory shock

Storage scaling note: For an elementary single decision cell (4 weights), standard Float32 requires 16 bytes compared to 24 bytes for OED (3 double-precision coordinates). The decisive storage advantage of OED (constant $O(1)$ vs. linear $O(W)$) manifests when scaling to multi-neuron architectures where fixed coordinate tuples parameterize synthetic layers without allocating tensor matrices (extrapolated in Fig. 7c).

Parametric Constraint & Robustness Analysis

Because OED parameterizes the 4-dimensional weight vector $W \in [-1, 1]^4$ through a 3-parameter coordinate tuple $\Theta = (c_x, c_y, \zeta)$ via the quadrant transform $w_i = 2R_i - 1$, the model operates under a strictly constrained 3-degree-of-freedom manifold. By first principles of statistical optimization, a constrained parametric model cannot surpass unconstrained backpropagation on unregularized training loss. The empirical significance of OED lies not in outperforming unconstrained gradient descent on convex metrics, but in achieving near-parity (within 7.00% on test data) while eliminating persistent floating-point tensor matrices from physical memory (constant $O(1)$ = 24 bytes vs. linear $O(W)$). Under heavy test-set distribution shifts ($\Delta x \sim \mathcal{N}(1.5, 0.5)$), unshielded coordinate updates degrade to 56.67% ± 6.24%; the CD4+ regulatory mask attenuates gradient shocks, preserving 66.67% ± 8.23% accuracy (+10.00% margin over unshielded OED).

Hyperparameter	Symbol	Value / Setting	Algorithmic Function & Role
Coordinate Learning Rate	η	0.05	Step size for finite-difference coordinate gradient updates
Finite Difference Step	δ	1.0×10^{-4}	Perturbation radius for empirical gradient estimation $\nabla_\Theta L$
Initial Coordinate Seed	Θ_0	(0.25, 0.18, 1.0)	Starting parameter seed in parameter space ($\zeta_0 = \log_{10}(\text{zoom}) = 1.0$)
Total Training Epochs	T	150	Iterative optimization budget across batch evaluations
Zinc Spark Jump Scale	γ_{spark}	0.08	Cauchy scale parameter for non-local saddle-point tunneling
Gradient Stall Threshold	ε_{tol}	1.0×10^{-3}	Stagnation condition triggering the perturbed jump operator
Error Floor Threshold	τ_{err}	0.35	Prevents triggering stochastic jumps when loss is already minimized
Orbital Homeostasis Weight	λ_{orb}	0.05	Regularization enforcing boundary escape target $N^* = 35$
Quadrant Diversity Weight	β	0.01	Variance regularization $\sigma_{fractal}$ penalizing degenerate uniform escape
CD4+ Mask Slope & Tolerance	α, $\tau_{tolerance}$	5.0, 0.25	Sigmoidal steepness and threshold for adaptive gradient gating
Sampling Resolution	N_{res}	32 × 32 (Train) / 128 × 128 (Test)	Quadrant pixel sampling grid for numerical escape integration

10. CONCEPTUAL HARDWARE ARCHITECTURE: PROPOSED ANALOG OPTICAL CO-PROCESSOR

While digital silicon requires iterative arithmetic loops, OED maps natively to conceptual analog optical computing at the speed of light (Wetzstein et al., 2020). This section outlines a proposed physical architecture for future experimental prototyping:

- **Spatial Light Modulator (SLM):** Phase-encodes the coordinate tuple $\Theta = (c_x, c_y, \zeta)$ onto a 532 nm coherent laser wavefront.
- **4f Optical Fourier Lens System:** Computes an instantaneous continuous 2D Fourier transform ($\Delta t \approx 10^{-12}$ s).
- **Polarization Boundary Filters:** Impose the cardioid cusp boundary cut-off ($c = 1/4$) purely in the optical domain.
- **Dark-Basin Photoreceptor Arrays:** Integrated CMOS sensors read non-divergent energy intensity, converting optical interference directly into synaptic activation currents.

11. MASTER ONTOLOGICAL MAPPING: NATURAL SYSTEMS TO CYBERNETIC FORMALISMS

Table 3 articulates the formal translation between biological/physical phenomena and their exact cybernetic roles within the OED framework.

Natural & Physical Phenomenon	Ontological Significance	Cybernetic & Mathematical Formalism
Multi-Agent Boundary Exploration	Decentralized non-linear phase exploration	Multi-polar parameter search with dynamic coordinate shifts
Homogeneous Enforcers	Rigid compliance forcing equilibrium	Isotropic gradient descent causing over-smoothing and collapse ($L \to 0$)
Edge of Chaos Balance	Equilibrium between flexibility and structure	Critical state balancing exploration and exploitation ($\lambda_z \approx 0$)
Scale-Free Neural Hubs	Hierarchical network coordination	Central coordinate routing hub governing parameter projection
Protective Sacrifice / Damping	Boundary preservation under stress	Early-stopping dissipative regularization absorbing divergence
Spurious Signal Rejection	Disregarding secondary harmonic reflections	Filter isolating primary non-linear attractors from high-frequency noise
Orthogonal Error Balance	Complementary error compensation	Orthogonal error cancellation synthesizing stable decision planes
Evolutionary Transition	Environmental pressure forcing new modalities	Dimensionality expansion ($D \to D$+1) triggered by boundary compression
Zero-Friction Boundary Surfing	Dynamic non-equilibrium persistence	Limit-cycle boundary surfing avoiding central Lyapunov attractor collapse
Mammalian Zinc Spark	Inorganic ion burst breaking metabolic dormancy	Heavy-tailed perturbed jump operator ($\Omega_{tunneling}$) escaping saddle traps

12. CONCLUSION & PRIOR ART DECLARATION

The classical paradigm of deep learning—allocating dense floating-point matrices in DRAM and forcing empirical error to zero—presents fundamental thermodynamic and architectural constraints. In this revised preprint (v2.0), we have formulated **Orbital Error Dynamics (OED)**, establishing that organic intelligence is an active, non-equilibrium resistance against dynamic attractor collapse. By generating parameters as ephemeral topological standing waves ($O(1)$) from the Mandelbrot boundary $\partial\mathscr{M}$, formalizing the Bent Sine Wave and the Observer Horizon geometry, deploying the Biomimetic Perturbed Jump Operator ($\Omega_{\text{tunneling}}$), and introducing enteric-cranial dual-brain cybernetics with adaptive CD4+ immune gating, OED establishes a rigorous, permanent prior art foundation for zero-storage procedural AI in neuromorphic and resource-constrained edge computing.

> **Patent Priority Notice:** The foundational procedural weight derivation architectures, the adaptive CD4+ immune gating mask mechanism, and the zero-storage hardware co-processor implementations disclosed in this work are subject to national patent application **TR 2026/016285** filed on September 22, 2026 at the Turkish Patent and Trademark Office (TÜRKPATENT).

REFERENCES

[1] V. Dağlı, Z. Dağlı, and D. Dağlı, "Mandelbrot Fractal Neural Synthesis: Zero-Storage Procedural Weight Derivation and Non-Linear Decision Boundaries," *Zenodo Research Repository*, DOI: 10.5281/zenodo.22867037, 2026.

[2] B. B. Mandelbrot, *The Fractal Geometry of Nature*. W. H. Freeman and Company, New York, 1982.

[3] E. Schrödinger, *What is Life? The Physical Aspect of the Living Cell*. Cambridge University Press, 1944.

[4] G. Nicolis and I. Prigogine, *Self-Organization in Nonequilibrium Systems: From Dissipative Structures to Order through Fluctuations*. John Wiley & Sons, New York, 1977.

[5] K. Friston, "The free-energy principle: a unified brain theory?" *Nature Reviews Neuroscience*, vol. 11, no. 2, pp. 127–138, 2010.

[6] P. Bak, C. Tang, and K. Wiesenfeld, "Self-organized criticality: An explanation of the 1/f noise," *Physical Review Letters*, vol. 59, no. 4, pp. 381–384, 1987.

[7] F. E. Duncan, T. K. Woodruff et al., "The zinc spark is an inorganic signature of human egg activation," *Scientific Reports*, vol. 6, p. 24737, 2016.

[8] C. Jin, R. Ge, P. Netrapalli, S. M. Kakade, and M. I. Jordan, "How to escape saddle points efficiently," in *International Conference on Machine Learning (ICML)*, pp. 1724–1732, PMLR, 2017.

[9] M. Horowitz, "1.1 Computing's energy problem (and what we can do about it)," in *IEEE International Solid-State Circuits Conference (ISSCC) Digest of Technical Papers*, pp. 9–14, 2014.

[10] R. Sender, S. Fuchs, and R. Milo, "Revised estimates for the number of human and bacteria cells in the body," *PLOS Biology*, vol. 14, no. 8, p. e1002533, 2016.

[11] I. Shumailov et al., "AI models collapse when trained on recursively generated data," *Nature*, vol. 631, pp. 755–759, 2024.

[12] J. B. Furness, "The enteric nervous system and neurogastroenterology," *Nature Reviews Gastroenterology & Hepatology*, vol. 9, pp. 286–294, 2012.

[13] S. Sakaguchi et al., "Regulatory T cells and immune tolerance," *Cell*, vol. 133, no. 5, pp. 775–787, 2008.

[14] G. Wetzstein et al., "Inference in artificial intelligence with deep optics and photonics," *Nature*, vol. 588, pp. 39–47, 2020.